# Analysis and Mitigation of Subsynchronous Resonance in Series-Compensated Grid-Connected System Controlled by a Virtual Synchronous Generator

Gaoxiang Li, Yandong Chen, *Senior Member, IEEE*, An Luo, *Senior Member, IEEE*, Zhixing He, *Member, IEEE*, Haining Wang, Zhen Zhu, Wenhua Wu, *Member, IEEE*, and Leming Zhou, *Member, IEEE*

***Abstract*—Analogizing the subsynchronous resonance (SSR) phenomenon of the series-compensated grid-connected system based on synchronous generator, the virtual synchronous generator (VSG) also has the low-frequency oscillation problem owing to the impedance interaction between VSG and series-compensated network. Stability of the series-compensated grid-connected system controlled by VSG is analyzed by the impedance-based Nyquist stability criterion. Due to the inductive impedance of VSG, VSG is easy to couple with the series-compensated network in the low-frequency areas, which can lead to the SSR. With the increase of the series compensation level, the stability of VSG becomes worse and the induced oscillation frequency becomes higher. Therefore, a modulation signal feedforward active-damping control strategy with time-delay compensation is proposed to suppress this SSR, which directly feeds the active-damping control signal to the pulsewidth modulation modulator for reshaping the output impedance of VSG from the inductance to the resistance–inductance. Moreover, a value range of virtual resistance is given with considering the influence on the regular operation of VSG. Finally, the simulation and experimental results verify the correctness of the SSR analysis and the feasibility of the proposed active-damping control strategy.**

***Index Terms*—Active-damping control, modulation signal feedforward, series-compensation level, subsynchronous resonance (SSR), virtual synchronous generator (VSG).**

## I. Introduction

RECENTLY, the renewable energy generation, especially wind and photovoltaic power generation, has developed rapidly. Generally, power stations based on renewable energy are widely located in remote areas, such as deserts and islands, and they are far away from the big cities [1]. To improve the transfer capability, the series-compensated transmission line is usually used in renewable energy generation [2], [3]. More and more power stations based on renewable energy are connected to the power grid, which causes a series of problems [4], [5]. Meanwhile, along with the development of renewable power generation, the control strategy of virtual synchronous generator (VSG) [6] is proposed by imitating the mechanism and external characteristics of the traditional synchronous generator (SG). Owing to the characteristics of voltage regulation and frequency modulation, VSG has become a research hotspot [7], [8], and it has been applied in renewable energy generation [9].

In addition, VSG can be categorized into the VSG with inner control loops and the VSG without inner control loops [10]. Compared with the VSG with inner control loops, the VSG without inner control loops [6] is simpler and more stable under weak grid [11]. Due to limited space, this article mainly studies the VSG without inner control loops, and the following VSG refers to the kind of VSG without inner control loops if there is no special explanation. Due to the excellent performance of VSG, there are many researchers and the stability of VSG under weak grid has been investigated from the point of view of the impedance [11], transfer function [12], and eigenvalue [13]. However, the stability of VSG under the series-compensated grid-connected situation has not been previously presented in the literature. Meanwhile, there is no paper to introduce the common problems between SG and VSG. Moreover, with the application of VSG in renewable energy generation, the situations where the VSG and series-compensated grid really exist, such as the battery storage inverter controlled by VSG in wind farm connected to the series-compensated transmission line. The impedance of VSG is basically inductive [14], which is similar to that of SG [15]. From the point of view of the impedance, the series-compensated grid-connected system controlled by VSG will have the similar subsynchronous resonance (SSR) problem occurred in the traditional series-compensated grid-connected system based on SG [16]. Therefore, it is necessary to study the stability of VSG under series-compensated grid-connected situation.

Manuscript received July 20, 2019; revised October 26, 2019 and January 8, 2020; accepted February 28, 2020. Date of publication March 3, 2020; date of current version June 23, 2020. This work was supported by the National Key Research and Development Program of China under Grant 2017YFB0902000. Recommended for publication by Associate Editor S. Golestan. *(Corresponding author: Yandong Chen.)*

The authors are with the College of Electrical and Information Engineering, Hunan University, Changsha 410082, China (e-mail: ligaoxiang5@163.com; yandong_chen@hnu.edu.cn; an_luo@126.com; hezhixingmail@163.com; wang_haining@yesh.net; 332120507@qq.com; wenhua_5@163.com; leming_zhou@126.com).

Color versions of one or more of the figures in this article are available online at http://ieeexplore.ieee.org.

Digital Object Identifier 10.1109/TPEL.2020.2977981

As the SSR will cause additional power losses and even result in system instability, it has aroused great concerns from both academic and industrial communities [17]. Currently, the SSR of wind farms connected to a series-compensated network is receiving more and more attention [18], [19]. A large number of scholars have studied this type of SSR and proposed various analysis methods [20], [21]. Meanwhile, with the development of impedance modeling, the impedance-based Nyquist stability criterion is applied to analyze the SSR phenomenon [22]. Since the sequence impedance model has the advantages of direct measurement and simple form, it has become an important way to analyze the interaction stability of inverter [23]. Owing to the phase-locked loop (PLL) and the asymmetric control in the *dq* coordinate, there exist couplings between the positive- and negative-sequence impedances [24]. Compared with the decoupling sequence impedance model, the sequence impedance model with considering couplings is more precise and can predict the exact stability boundary [25], [26]. However, when the study does not focus on the problem of system stability boundary, the decoupling sequence impedance model is usually accurate enough to analyze the mechanism and characteristics of system oscillation [27], [28]. In addition, on the issue of SSR analysis, frequency scanning is a general way no matter for the traditional power generation systems or the renewable energy generation systems. For the frequency scanning method, the impedance couplings are not considered and it usually only uses the positive-sequence impedance [29]. Since the used VSG neither needs PLL nor works in the *dq* coordinate, the sequence impedance couplings should be small. Meanwhile, considering the successful applications of the decoupling sequence impedance on SSR analysis [27]–[30], the decoupling sequence impedance of VSG can be utilized to analyze the mechanism and characteristics of SSR.

Moreover, the suppression methods of SSR can be divided into two categories: one is to add additional equipment [31], and the other is to improve the control strategy [32]. Compared with the suppression method of adding additional equipment, it is more economical to suppress SSR by improving the control strategy. Because the output voltage of VSG can be directly controlled, the methods of implementing damping control for VSG are more flexible than that of SG. In addition, the performance of VSG should not be changed after improving the control strategy. Based on the virtual impedance control of the traditional grid-connected inverter [33], the virtual impedance controls of VSG are presented in [34]–[36]. In [34], a virtual resistance is proposed to improve the efficiency of VSG by replacing the real resistance in the power circuit. In [12], [13], and [35], the virtual impedance controls are presented to improve the stability of VSG under the weak grid. In [36], a harmonic virtual impedance is designed for suppressing harmonics. As the virtual impedance control of VSG will influence its regular operation, the virtual impedance has a value range. However, the abovementioned studies do not consider the value range of virtual impedance.

This article studied the stability of the series-compensated grid-connected system controlled by VSG, and revealed an SSR phenomenon caused by the impedance interaction between VSG and series-compensated network. To suppress this SSR, a modulation signal feedforward active-damping control strategy with time-delay compensation is proposed. Meanwhile, to maintain the regular operation of VSG, the value range of virtual impedance is given. This article is organized as follows. In Section II, the reason why the VSG under the series-compensated grid-connected situation occurs SSR is analyzed in detail. In Section III, the mechanism of the proposed damping control for SSR is introduced. Experimental results are illustrated in Section IV. Finally, the conclusion is drawn in Section V.

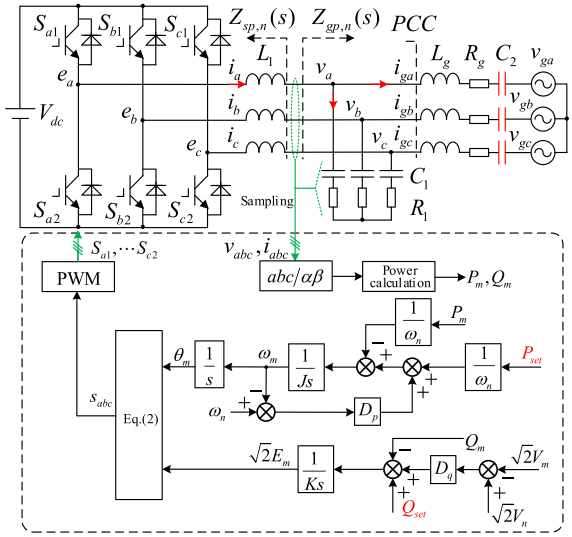


Fig. 1. Configuration and control structure of the series-compensated grid-connected system controlled by VSG.

## II. SSR Analysis of Series-Compensated Grid-Connected System Controlled by VSG

### A. Impedance of VSG With Different Control Parameters

The configuration and control structure of the series-compensated grid-connected system controlled by VSG are showed in Fig. 1, where $V_{\rm dc}$ is the dc-side voltage; $e_a$, $e_b$, and $e_c$ are the inner electric potentials of VSG; $i_a$, $i_b$, and $i_c$ are the currents of filter inductance $L_1$; $v_a$, $v_b$, and $v_c$ are the point of common coupling (PCC) voltages; $i_{ga}$, $i_{gb}$, and $i_{gc}$ are the grid currents; $v_{ga}$, $v_{gb}$, and $v_{gc}$ are the grid voltages; $\mathrm{Z}_{sp,n}(\mathrm{s})$ are the positive- and negative-sequence impedances of VSG; $\mathrm{Z}_{gp,n}(\mathrm{s})$ are the positive- and negative-sequence impedances of the series-compensated network, which is composed of the series-compensated transmission line, filter capacitance $C_1$, and damping resistance $R_1$; $R_{\rm g}$, $L_{\rm g}$, and $C_2$ are the resistance, inductance, and capacitance of the series-compensated transmission line, respectively.

As seen from Fig. 1, the mathematical expression of VSG [7] can be expressed as follows:

$$\begin{cases} Q_{\rm set}+\sqrt{2}D_q\left(V_n-V_m\right)-Q_m=K\frac{d\left(\sqrt{2}E_m\right)}{dt} \\ T_{\rm set}+D_p\left(\omega_n-\omega_m\right)-T_e=J\frac{d\omega_m}{dt} \\ P_{\rm set}=T_{\rm set}\omega_m\approx T_{\rm set}\omega_n \\ P_m=T_e\omega_m\approx T_e\omega_n \\ \theta_m=\int\omega_m dt \end{cases} \tag{1}$$

where $J$ is the virtual moment of inertia; $\omega_m$ and $\omega_n$ are the output angular frequency and the rated angular frequency, respectively; $T_e$ and $T_{\rm set}$ are the electromagnetic torque and the electromagnetic torque reference, respectively; $P_m$ and $P_{\rm set}$ are the output active power and the active power reference, respectively; $Q_m$ and $Q_{\rm set}$ are the output reactive power and the reactive power reference, respectively; $K$ is the reactive inertia coefficient; $D_p$ and $D_q$ are the active droop coefficient and the reactive droop coefficient, respectively; and $\theta_m$ is the obtained phase angle of VSG. $V_m$ and $V_n$ are the rms value and the rated rms value of the PCC voltage, respectively; and $E_m$ is the rms value of the inner electric potential reference for VSG.

The modulation signals of VSG are determined by the active and reactive controllers, and they can be expressed as follows:

$$\begin{cases} s_a = 2\sqrt{2}E_m\cos\theta/V_{\rm dc} \\ s_b = 2\sqrt{2}E_m\cos\left(\theta-2\pi/3\right)/V_{\rm dc} \\ s_c = 2\sqrt{2}E_m\cos\left(\theta+2\pi/3\right)/V_{\rm dc} \end{cases} \tag{2}$$

where the $s_a$, $s_b$, and $s_c$ are the modulation signals of VSG.

According to Fig. 1, the following equation is derived:

$$L_1 s\begin{bmatrix} i_a \\ i_b \\ i_c \end{bmatrix} = \begin{bmatrix} e_a \\ e_b \\ e_c \end{bmatrix} - \begin{bmatrix} v_a \\ v_b \\ v_c \end{bmatrix}. \tag{3}$$

Based on the harmonic linearization method, the sequence impedance model of VSG can be built. According to [14], the positive- and negative-sequence impedances of VSG can be expressed as follows:

$$\begin{cases} Z_{sp}(s) = \frac{0.75V_1M(s-j2\pi f_r)K_d(s)e^{j\theta_d}/\omega_n+sL_1}{1+0.75I_1M(s-j2\pi f_r)K_d(s)e^{j(\theta_d-\theta_{ir})}/\omega_n} \\ Z_{sn}(s) = \frac{0.75V_1M(s+j2\pi f_r)K_d(s)e^{-j\theta_d}/\omega_n+sL_1}{1+0.75I_1M(s+j2\pi f_r)K_d(s)e^{-j(\theta_d-\theta_{ir})}/\omega_n} \end{cases} \tag{4}$$

where $Z_{sp,n}(\rm s)$ are the frequency-domain expressions of the positive- and negative-sequence impedances of VSG; $\theta_d = \arcsin\left[P_m\omega_nL_1/(E_mV_1)\right]+\pi/2$ and $\arcsin\left[P_m\omega_nL_1/(E_mV_1)\right]$ is the power angle of VSG; $M(\rm s) = 1/(Js^2+D_ps)$; $K_d(\rm s)$ is expressed as follows:

$$K_d(s) = \sqrt{2}E_me^{-1.5T_ss}/\left[(1+s/\omega_v)(1+s/\omega_i)\right] \tag{5}$$

where $T_s$ is the switching period; $\omega_v$ and $\omega_i$ are the cutoff frequency of the low-pass filter for the voltage and current signals, respectively.

According to (4), the impedance characteristics of VSG are affected by the control parameters $J$ and $D_p$. In addition, according to [7], the control parameters of the active power loop and the reactive power loop can be designed independently, and the active droop coefficient $D_p$ is as follows:

$$D_p(s) = \frac{\Delta T_{\max}}{\Delta\omega_{\max}} = \frac{\Delta P_{\max}}{\omega_n\Delta\omega_{\max}}. \tag{6}$$

According to (6), the active droop coefficient $D_p$ is determined by $\delta P_{\max}$ and $\delta\omega_{\max}$. Therefore, the selection range of $D_p$ is smaller. Similarly, the virtual inertia $J$ is designed according to the open-loop gain of active power, which is obtained by ignoring the coupling items between the active power loop and the reactive power loop. According to [7], the open-loop gain of active power can be expressed as follows:

$$T_p(s) = \frac{3V_gE_n}{\omega_nX_s}\frac{1}{Js^2+D_ps} \tag{7}$$

where $V_g$ is the rms value of grid voltage and $E_n$ is the rms value of the inner electric potentials of VSG. The virtual inertia $J$ is designed according to the bandwidth of $T_p(\rm s)$.

TABLE I
PARAMETERS OF CIRCUIT AND CONTROLLER

| Parameter | Value | Parameter | Value |
|---|---|---|---|
| $V_{dc}$/V | 700 | $f_n$/Hz | 50 |
| $L_1$/mH | 3 | $f_s(1/T_s)$/kHz | 10 |
| $C_1$/μF | 20 | $\omega_n$/(rad/s) | 100π |
| $R_1$/Ω | 1.73 | $\omega_v$/(rad/s) | 8000π |
| $L_g$/mH | 10 | $\omega_i$/(rad/s) | 8000π |
| $R_g$/Ω | 0.15 | $V_1$/V | 311 |
| $C_2$/F | 0.002 | $D_p$ | 5 |
| $v_{gabc}$/V | 220 | $D_q$ | 321 |
| $P_n$/kW | 10 | $K$ | 7.1 |
| $Q_n$/kVar | 0 | $J$ | 0.057 |

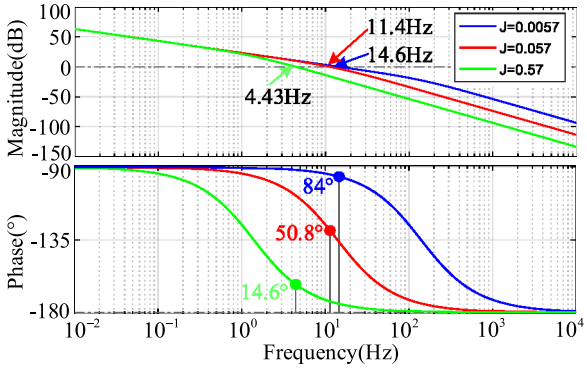


Fig. 2. Bode diagram of $T_p(\rm s)$ with different $J$.

Table I illustrates the main circuit and control parameters of Fig. 1. Fig. 2 shows the bode diagram of $T_p(\rm s)$ with different values of $J$. As seen in Fig. 2, the virtual inertia $J$ has a great influence on the phase margin of active power loop $T_p(\rm s)$. Therefore, considering the stability margin, the selection range of parameter $J$ is smaller. In addition, because the characteristics of the positive- and negative-sequence impedances are similar, it is sufficient to reflect the influence of the control parameters on the impedance of VSG by analyzing the positive-sequence impedance.

Fig. 3 shows the positive-sequence impedance of VSG with different control parameters. As seen in Fig. 3(a), the virtual inertia $J$ has a certain influence on the positive-sequence impedance of VSG in the low-frequency areas, and the corresponding phase of the positive-sequence impedance is bigger when $J$ is smaller. As seen in Fig. 3(b), the active droop coefficient $D_p$ mainly influence the positive-sequence impedance characteristics of VSG near the fundamental frequency, and the range of capacitance characteristics for the positive-sequence impedance is smaller when $D_p$ is bigger. It can be seen in Fig. 3 that the virtual

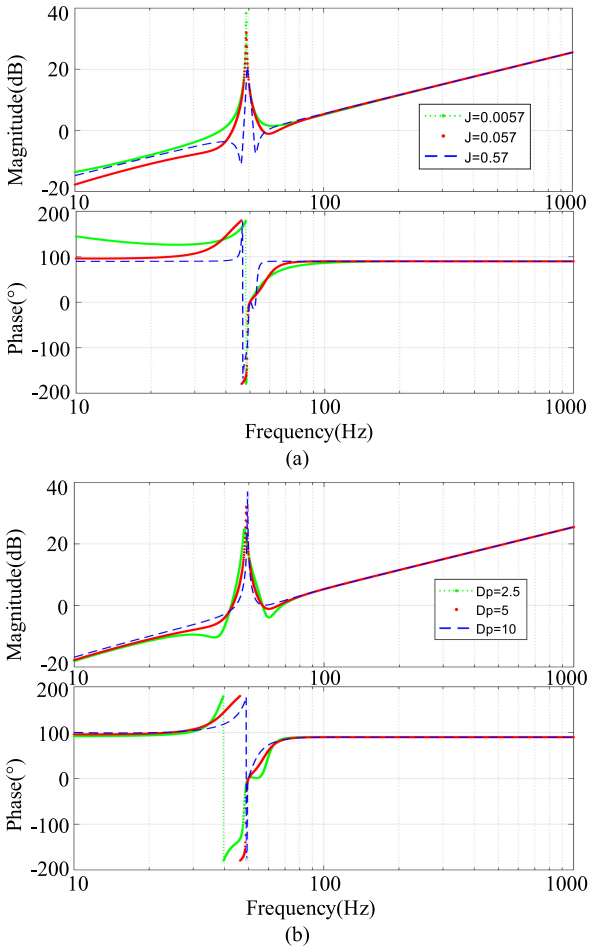


Fig. 3. Positive-sequence impedance of VSG with different control parameters. (a) Different *J*. (b) Different $D_p$.

inertia *J* and active droop coefficient $D_p$ have a certain influence on the impedance characteristics of VSG, and the impedance characteristics of VSG with different control parameters are also basically unchanged, which are basically the inductive impedance characteristics.

For the series-compensated transmission line, the series-compensation level (SCL) can be obtained as follows:

$$\mathrm{SCL} = \frac{1}{\omega_n^2 L_g C_2}. \tag{8}$$

As seen in Fig. 1, the impedance expression of the series-compensated network can be obtained as follows:

$$Z_g(s) = [sL_g + R_g + 1/(sC_2)] \,||\, [R_1 + 1/(sC_1)] \tag{9}$$

where $Z_g(\mathrm{s})$ is the frequency-domain expression of the series-compensated network. When the grid-connected system is completely symmetrical, the positive- and negative-sequence impedances of the series-compensated network can be expressed as $\mathrm{Z}_{gp}(s) = \mathrm{Z}_{gn}(s) = \mathrm{Z}_g(s)$.

Fig. 4 shows the frequency response characteristics of the positive- and negative-sequence impedances of VSG and series-compensated network with different SCLs. As seen in Fig. 4,

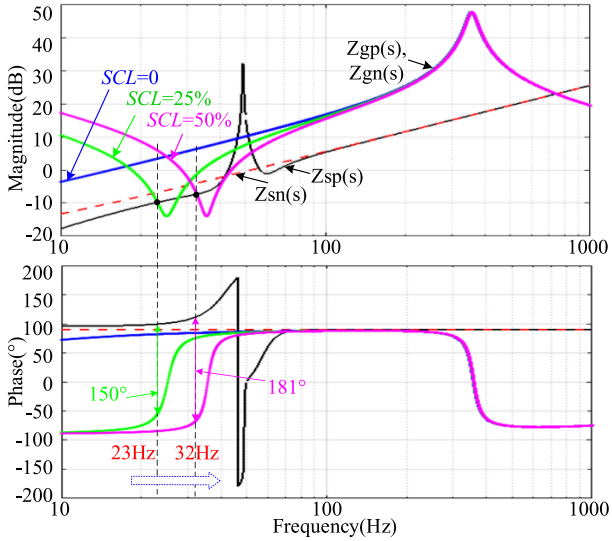


Fig. 4. Sequence impedances of VSG and series-compensated network.

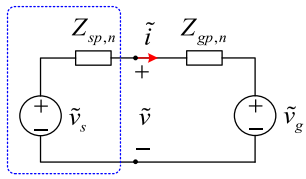


Fig. 5. Thevenin equivalent circuit of the small-signal series-compensated grid-connected system controlled by VSG.

when SCL = 0, $Z_{gp,n}(\mathrm{s})$ do not intersect $Z_{sp}(\mathrm{s})$ in the low-frequency areas; when SCL = 25%, $Z_{gp,n}(\mathrm{s})$ intersect $Z_{sp}(\mathrm{s})$ at 23 Hz and the corresponding phase difference is 150°; when SCL = 50%, $Z_{gp,n}(\mathrm{s})$ intersect $Z_{sp}(\mathrm{s})$ at 32 Hz and the corresponding phase difference is 181°. From Fig. 4, with the increase of the SCL, the intersection point between $Z_{gp,n}(\mathrm{s})$ and $Z_{sp}(\mathrm{s})$ shifts to the high-frequency areas and the corresponding phase difference increases to more than 180°. Because the series-compensated network is capacitive in the low-frequency areas and there is a downward bulge for the impedance magnitude, it easily couples with the VSG at the intersection point of the impedance magnitude.

### *B. Small-Signal Stability Analysis*

According to Fig. 1, the Thevenin equivalent circuit of the small-signal series-compensated grid-connected system controlled by VSG is depicted in Fig. 5, where $\tilde{v}_s$ and $\tilde{v}_g$ are the ideal voltage source of the Thevenin equivalent circuit of the VSG and the grid, respectively.

From Fig. 5, the small-signal grid-connected current $\tilde{i}$ can be obtained as follows:

$$\tilde{i} = \frac{\tilde{v}_s - \tilde{v}_g}{Z_{gp,n}} \frac{1}{1 + Z_{sp,n}/Z_{gp,n}}. \tag{10}$$

Both VSG and grid can run independently and stably. Therefore, voltages $\tilde{v}_s$ and $\tilde{v}_g$ are stable because they are the ideal voltage sources of the Thevenin equivalent circuit of the VSG and the

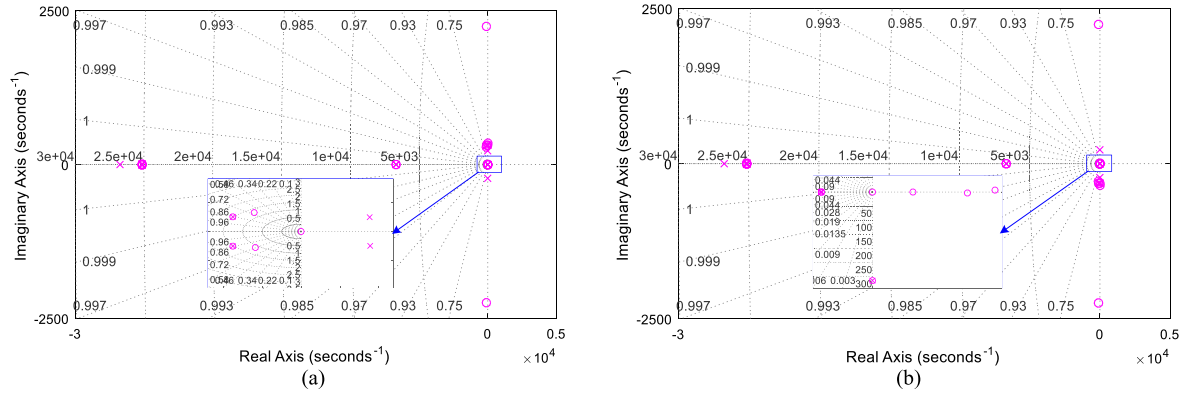


Fig. 6. Pole-zero maps of (a) $G_{rp}(\mathrm{s})$ and (b) $G_{rn}(\mathrm{s})$.

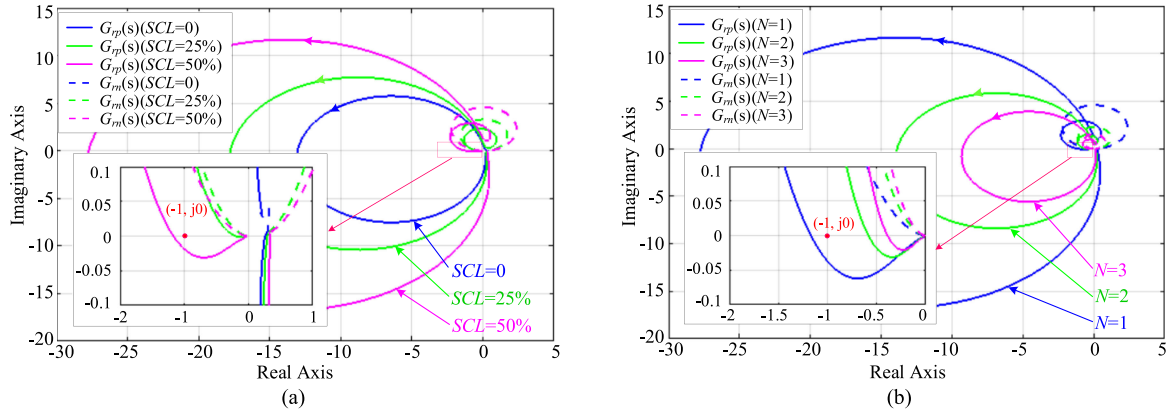


Fig. 7. Nyquist plots of (11) with different parameters. (a) Different SCLs. (b) Different number $N$ of parallel VSGs when SCL = 50%.

grid, respectively. In addition, since $Z_{gp,n}$ are grid impedances and the grid can run stably, $1/Z_{gp,n}$ is stable too. Based on the analysis above, the stability of the series-compensated grid-connected system controlled by VSG is determined by $1/(1+\mathrm{Z}_{sp,n}/\mathrm{Z}_{gp,n})$.

For the grid-connected inverter, the Nyquist stability criterion based on the impedance ratio is usually used for analyzing the system stability. To analyze the influences of other parameters on system stability, the impedance ratio of the series-compensated grid-connected system controlled by VSG can be obtained as follows:

$$\begin{cases} G_{rp}(s) = Z_{sp}(s)/Z_{gp}(s) \\ G_{rn}(s) = Z_{sn}(s)/Z_{gn}(s). \end{cases} \tag{11}$$

According to (11), the pole-zero maps of $G_{rp}(\mathrm{s})$ and $G_{rn}(\mathrm{s})$ are depicted in Fig. 6, and the Nyquist plots of (11) with different parameters are depicted in Fig. 7.

As seen in Fig. 6, the impedance ratio $G_{rp}(\mathrm{s})$ has two poles in the right-half-plane (RHP), and $G_{rn}(\mathrm{s})$ has no pole in the RHP. Therefore, when the series-compensated grid-connected system controlled by VSG is stable, the $G_{rp}(\mathrm{s})$ should encircle $(-1,$ $j0)$ point once in the counterclockwise direction, and the $G_{rn}(\mathrm{s})$ should not encircle the $(-1,$ $j0)$ point. As seen in Fig. 7(a), when the SCL is increased from 25% to 50%, the Nyquist plots of $G_{rp}(\mathrm{s})$ cross the negative real axis from the right side to the left side of $(-1, j0)$ point, and the Nyquist plots of $G_{rn}(\mathrm{s})$ do not encircle the $(-1, j0)$ point. Therefore, the series-compensated grid-connected system controlled by VSG is unstable when SCL = 50%. When the SCL is higher, the capacitance characteristic range of the impedance of the series-compensated network is bigger, which can cause the impedance interaction between VSG and series-compensated network. As seen in Fig. 7(b), when SCL = 50% and the number $N$ of parallel VSGs increases, the Nyquist plots of $G_{rp}(\mathrm{s})$ cross the negative real axis from the original left side to the right side of $(-1, j0)$ point, and the Nyquist plots of $G_{rn}(\mathrm{s})$ do not encircle the $(-1, j0)$ point. So, the corresponding system changes from unstable to stable. When the number $N$ of parallel VSGs increases, the parallel impedance of VSGs decreases, and the impedance magnitude difference of the parallel VSGs and series-compensated network becomes bigger. Therefore, VSGs and series-compensated network are not easy to couple and the system stability becomes better. From Fig. 7, with the increase of the SCL, the stability of the series-compensated grid-connected system controlled by VSG becomes worse; with the increase of the parallel VSGs, the stability of the series-compensated grid-connected system controlled by VSG becomes stronger.

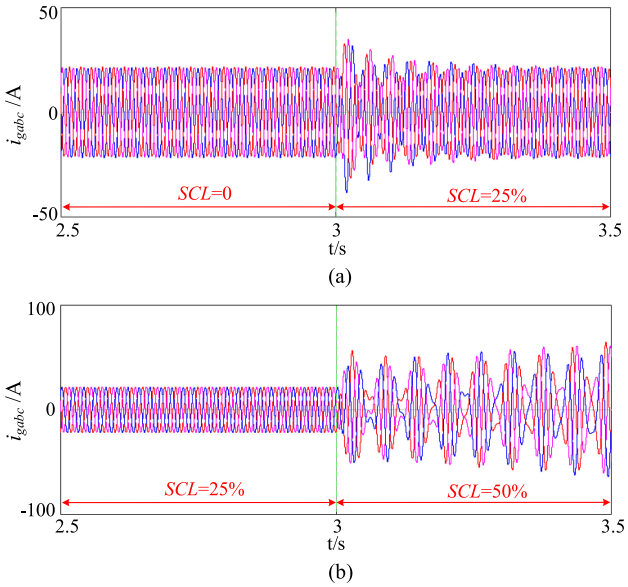


Fig. 8. Simulation results with different conditions. (a) SCL is increased from 0 to 25%. (b) SCL is increased from 25% to 50%.

In order to verify the correctness of theoretical analysis, a series-compensated grid-connected system controlled by VSG, as shown in Fig. 1, is simulated in MATLAB/Simulink, and the simulation results are shown in Fig. 8.

As seen in Fig. 8(a), when the SCL is increased from 0 to 25%, the grid-connected currents $i_{gabc}$ first occur low-frequency oscillation and then stabilize. As seen in Fig. 8(b), when the SCL is increased from 25% to 50%, the grid-connected currents $i_{gabc}$ appear low-frequency oscillation, and the series-compensated grid-connected system controlled by VSG changes from stable to unstable. Fig. 9 shows the current spectrums of $i_{gabc}$ in Fig. 8. As seen in Fig. 9(a), when the SCL is increased from 0 to 25%, the induced oscillation frequency of the system is mainly at 23 Hz. As seen in Fig. 9(b), when the SCL is increased from 25% to 50%, the induced oscillation frequency of the system is mainly at 32 Hz. The simulation results are consistent with the theoretical analysis and verify the correctness of theoretical analysis. Based on the analysis mentioned above, with the increase of SCL, the series-compensated grid-connected system controlled by VSG changes from stable to unstable. In addition, when the SCL is bigger, the induced oscillation frequency is higher.

## III. Modulation Signal Feedforward Active-Damping Control Strategy With Time-Delay Compensation for Mitigating the SSR

In order to mitigate the SSR caused by the impedance interaction between the VSG and the series-compensated network, a modulation signal feedforward active-damping control strategy with time-delay compensation is proposed. Fig. 10 shows the control diagram of the proposed modulation signal feedforward active-damping control. In Fig. 10, $\triangle s_{abc}$ are the feedforward values of the modulation signals, and $H_1(s)$ is the transfer function from $i_{abc}$ to $\triangle s_{abc}$. By the equivalent transformation,

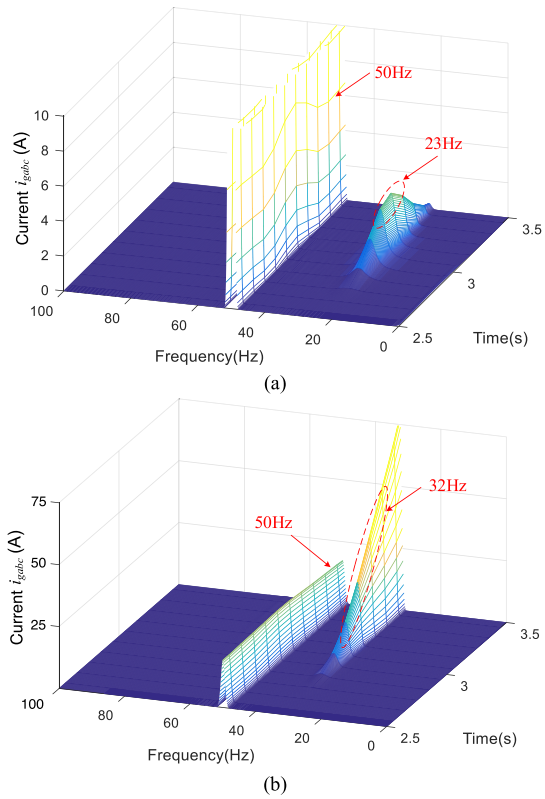


Fig. 9. Current spectrums of $i_{gabc}$ in Fig. 8. (a) SCL is increased from 0 to 25%. (b) SCL is increased from 25% to 50%.

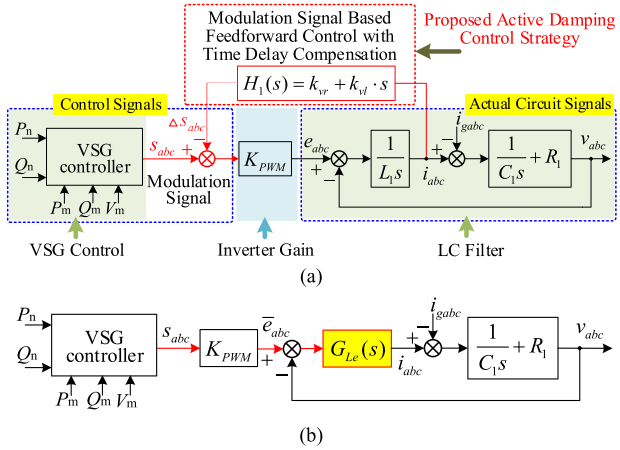


Fig. 10. Proposed modulation signal feedforward active-damping control strategy with time-delay compensation. (a) Proposed active-damping control diagram. (b) Equivalent control diagram.

the control diagram of the proposed modulation signal based active-damping control can be simplified as Fig. 10(b), where $\bar{e}_{abc}$ is the virtual inner electric potential of VSG and $G_{Le}(s)$ is the equivalent transfer function of the proposed active-damping control and filter inductance $L_1$.

According to Fig. 10, $G_{Le}(s)$ can be obtained and expressed as follows:

$$G_{Le}(s) = \frac{1}{sL_1 + H_1(s)K_{\mathrm{PWM}}} \tag{12}$$

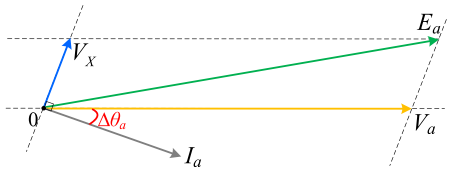


Fig. 11. Vector diagrams of $v_a$, $e_a$, $v_x$ and $i_a$.

where $H_1(s) = k_{vr} + k_{vl} \cdot s$ is the proposed active-damping controller. $k_{vr}$ and $k_{vl}$ are the control parameters that need to be designed. In addition, $k_{vr}$ and $k_{vl}$ have the following relationship:

$$\frac{k_{vl}}{k_{vr}} = 1.5T_s. \tag{13}$$

Considering the time delay of inverter, the inverter gain $K_{\mathrm{PWM}}$ can be expressed as follows:

$$K_{\mathrm{PWM}} = \frac{V_{\mathrm{dc}}}{2} e^{-1.5T_s s} \approx \frac{V_{\mathrm{dc}}}{2} \frac{1}{1 + 1.5T_s s}. \tag{14}$$

Substituting (13) and (14) into (12), (12) can be simplified, and expressed as follows:

$$\begin{cases} G_{Le}(s) \approx \frac{1}{sL_1 + R_v} \\ R_v = k_{vr} V_{\mathrm{dc}}/2 \end{cases} \tag{15}$$

where $R_v$ is the virtual equivalent resistor of the proposed active-damping control.

According to (15), the proposed active-damping control is equivalent to adding a virtual series resistor for the filter inductor $L_1$. According to Fig. 10 and (15), (3) can be rewritten as follows:

$$L_1 s \begin{bmatrix} i_a \\ i_b \\ i_c \end{bmatrix} + R_v \begin{bmatrix} i_a \\ i_b \\ i_c \end{bmatrix} = \begin{bmatrix} e_a \\ e_b \\ e_c \end{bmatrix} - \begin{bmatrix} v_a \\ v_b \\ v_c \end{bmatrix}. \tag{16}$$

Since the virtual resistance only causes a change within the control system and does not affect the physical circuit, the value of the virtual resistor $R_v$ will not influence the limit of the overmodulation for converter. In addition, considering the voltage drop control of VSG, current $i_a$ may not remain in phase with voltage $v_a$. According to Fig. 1, the vector diagrams of $v_a$, $e_a$, $v_x$, and $i_a$ are depicted in Fig. 11, where $v_x$ is the voltage on the filter inductor $L_1$; $V_a$, $E_a$, $I_a$, and $V_x$ are the rms values of $v_a$, $e_a$, $i_a$ and $v_x$, respectively; and $\triangle\theta_a$ is the phase difference between $V_a$ and $I_a$.

As the rated reactive power $Q_n = 0$, there is

$$\tan(\Delta\theta_a) = \frac{Q_m}{P_m} \approx \frac{Q_m}{P_n}. \tag{17}$$

According to Fig. 11, the value of $E_a$ can be obtained as follows:

$$E_a = \sqrt{(V_a + V_X \sin\Delta\theta_a)^2 + (V_X \cos\Delta\theta_a)^2} \tag{18}$$

where the $V_x = I_a \omega_n L_1$.

In addition, with considering the overmodulation problem, the maximum value of $E_a$ is obtained as follows:

$$E_{a\_\max} = \frac{\sqrt{2} V_{\mathrm{dc}}}{4}. \tag{19}$$

Usually, the voltage droop is smaller than 5% [7]. According to (1), (17), and (18), $E_a$ is equivalent to 234 V when the voltage droop is 5%, which is smaller than $E_{a\_\max}$ (246.2V). Therefore, the VSG will not normally appear overmodulation induced by the voltage droop.

Moreover, to better evaluate the value of $R_v$, a power correction ratio $\xi$ is defined as follows:

$$\xi = \frac{P_{Rv}}{P_n} \approx \frac{3I_a^2 R_v}{3V_a I_a} = \frac{I_a R_v}{V_a} \tag{20}$$

where $P_{Rv}$ is the virtual active power induced by the virtual resistor $R_v$.

Generally, with the increase of the virtual active power $P_{Rv}$, the differences between the control system with and without the virtual impedance control become big, which is similar to the work-point-offset problem of the controller and can cause the change of the regular operation for VSG. Since the virtual active power $P_{Rv}$ is directly proportional to the virtual resistor $R_v$, the influence of the proposed active-damping control on the regular operation of VSG will enhance with the increase of the virtual resistor $R_v$. Therefore, to maintain the regular operation of VSG, the power correction ratio $\xi$ should not be big. Usually, the influence of virtual impedance control on the regular operation of the system can be ignored when the change of controller is small. Therefore, the expected range of the virtual resistance is that the corresponding power correction ratio $\xi$ should not be big, such as 5%. Based on the analysis above, the virtual resistor is set to be 0.7 Ω, and the corresponding power correction ratio $\xi$ is 4.8%, which is lower than 5%.

According to (4) and (16), after adding the proposed active-damping control, the frequency response characteristics of the positive- and negative-sequence impedances of VSG can be obtained as follows:

$$\begin{cases} Z_{esp} = \frac{0.75V_1 M(s - j2\pi f_1) K(s) e^{j\theta_d}/\omega_n + sL_1 + R_v}{1 + 0.75V_m M(s - j2\pi f_1) K(s) e^{j(\theta_d - \theta_{ir})}/\omega_n} \\ Z_{esn} = \frac{0.75V_1 M(s + j2\pi f_1) K(s) e^{-j\theta_d}/\omega_n + sL_1 + R_v}{1 + 0.75V_1 M(s + j2\pi f_1) K(s) e^{j(\theta_{ir} - \theta_d)}/\omega_n}. \end{cases} \tag{21}$$

Fig. 12 shows the frequency response characteristics of the positive- and negative-sequence impedances of VSG with the proposed active-damping control. As seen in Fig. 12, with the increase of $R_v$, the magnitudes of the impedances $\mathrm{Z}_{sp,n}(\mathrm{s})$ increase obviously in the low-frequency areas, and the corresponding phases of impedances $\mathrm{Z}_{sp,n}(\mathrm{s})$ decrease significantly. In addition, the intersection point of impedances $\mathrm{Z}_{gp,n}(\mathrm{s})$ and $\mathrm{Z}_{sp,n}(\mathrm{s})$ shifts to the low-frequency areas, and the corresponding phase difference gradually decreases to less than 180°. From Fig. 12, because the proposed active-damping control is equivalent to adding a virtual series resistor $R_v$ for the filter inductor $L_1$, the impedance of VSG is reshaped from the inductance to the resistance–inductance. In addition, when the value of $R_v$ is bigger, the inductive impedance characteristics of $Z_{sp,n}(\mathrm{s})$ are weaker in the low-frequency areas.

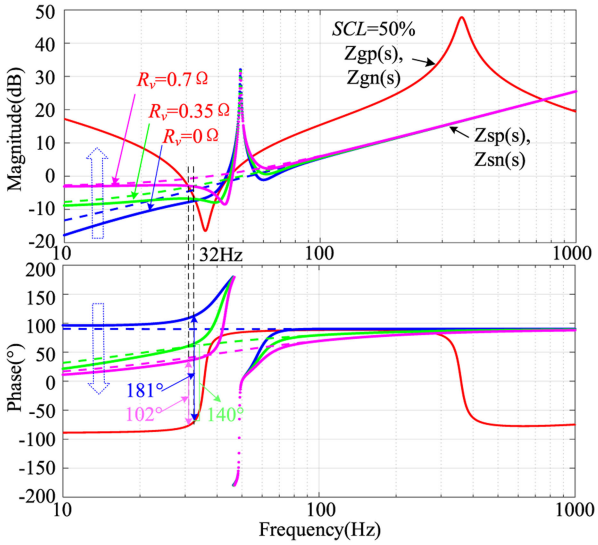


Fig. 12. Sequence impedances of the VSG with proposed active-damping control.

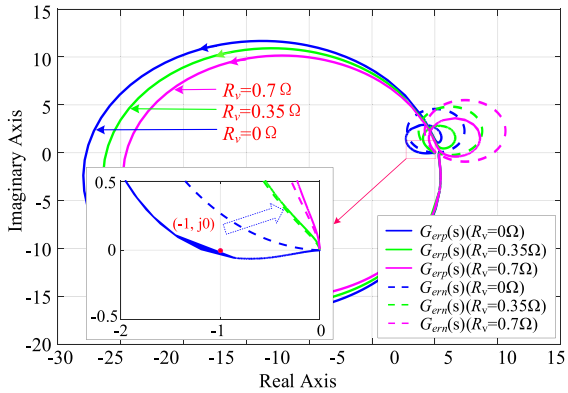


Fig. 13. Nyquist plots of (22).

According to (9) and (21), after adding the proposed active-damping control, the new impedance ratio can be expressed as follows:

$$\begin{cases} G_{erp}(s) = Z_{esp}(s)/Z_{gp}(s) \\ G_{ern}(s) = Z_{esn}(s)/Z_{gn}(s). \end{cases} \tag{22}$$

The impedance ratios $G_{erp,n}(\mathrm{s})$ are similar to $G_{rp,n}(\mathrm{s})$. $G_{erp}(\mathrm{s})$ have two poles in the RHP and $G_{ern}(\mathrm{s})$ have no pole in the RHP. Therefore, when the system is stable, the $G_{erp}(\mathrm{s})$ should encircle $(-1, j0)$ point once in the counterclockwise direction, and the $G_{ern}(\mathrm{s})$ should not encircle $(-1, j0)$ point. Fig. 13 shows the Nyquist plots of (22) when SCL = 50%. As seen in Fig. 13, after adding the proposed active-damping control, the Nyquist plots of $G_{erp}(\mathrm{s})$ cross the negative real axis from the left side to the right side of $(-1, j0)$ point, and the Nyquist plots of $G_{ern}(\mathrm{s})$ do not encircle the $(-1, j0)$ point. Therefore, by adding the proposed active-damping control, the series-compensated grid-connected system controlled by VSG changes from unstable to stable when SCL = 50%. With the increase of $R_v$, the resistance characteristic of the impedance of VSG becomes stronger. Therefore, the stability of the series-compensated grid-connected system controlled by VSG becomes better with the increase of $R_v$.

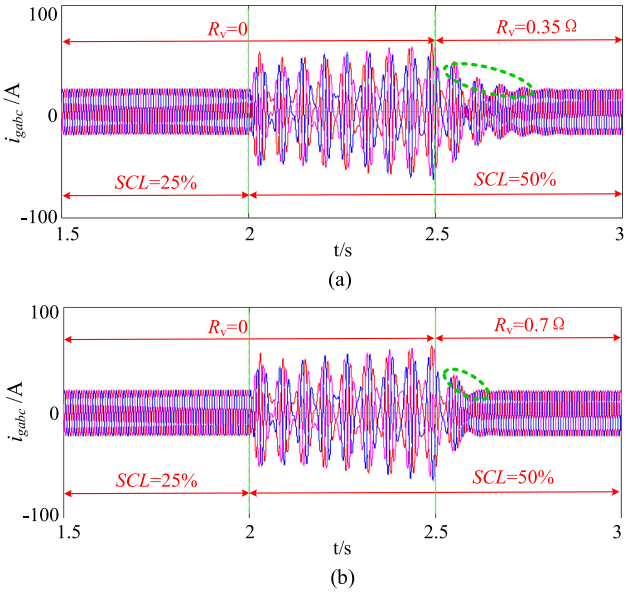


Fig. 14. Simulation results with different values of $R_v$. (a) $R_v = 0.35\ \Omega$. (b) $R_v = 0.7\ \Omega$.

To prove the validity of the proposed active-damping control strategy for suppressing the SSR, a series-compensated grid-connected system, as shown in Fig. 1, is simulated in MATLAB/Simulink, and the simulation results are shown as follows.

As seen from Fig. 14, with the proposed active-damping control, the SSR can be damped gradually, and the series-compensated grid-connected system controlled by VSG can keep stable at last. Moreover, the adjustment time of the system is shorter when the virtual resistor $R_v$ is bigger. As seen in Fig. 14, when $R_v$ is bigger, the oscillation damping ability of the system is stronger. Based on the analysis mentioned above, the proposed active-damping control strategy can effectively suppress the SSR in the series-compensated grid-connected system controlled by VSG. In addition, with the increase of $R_v$, the oscillation damping ability of the system becomes stronger.

## IV. Experimental Results

To validate the correctness of the SSR analysis and the feasibility of the proposed active-damping control strategy, a prototype for grid-connected inverter with series-compensation capacitor is built in lab for verification, and the proposed control strategy is implemented in TMS320F28335. Moreover, a low-pass filter is used to avoid the amplification of noise caused by the derivative term of the proposed controller. Fig. 15 gives the experimental platform of the series-compensated grid-connected system controlled by VSG. The parameters of the circuit and controller are listed in Table I. The experimental results are shown as follows.

Fig. 16 shows the experimental results of the impedance measurement without the proposed active-damping control.

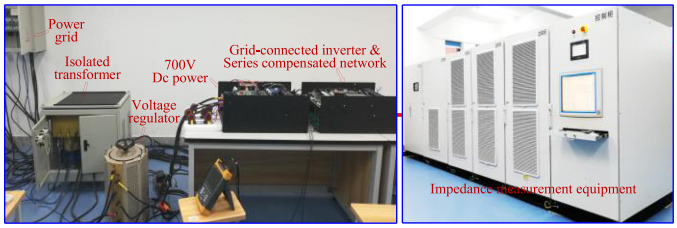


Fig. 15. Experimental platform.

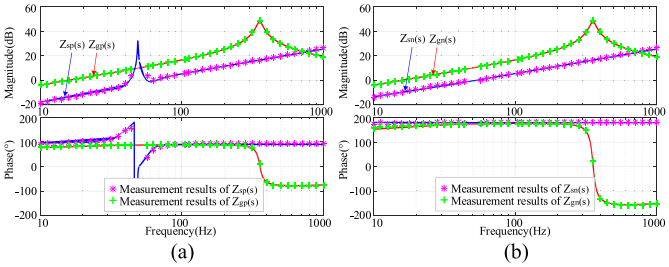


Fig. 16. Experimental results of impedance measurement without the proposed active-damping control. (a) Measurement results of $Z_{sp}(s)$ and $Z_{gp}(s)$ when SCL = 0. (b) Measurement results of $Z_{sn}(s)$ and $Z_{gn}(s)$ when SCL = 0.

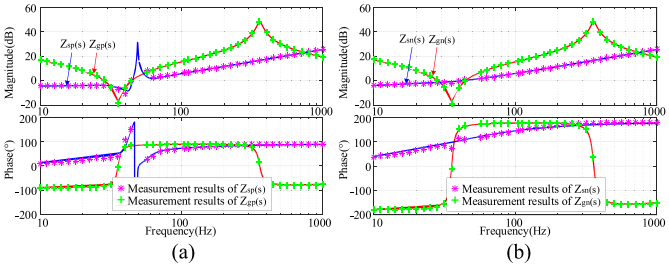


Fig. 17. Experimental results of impedance measurement with the proposed active-damping control. (a) Measurement results of $Z_{sp}(s)$ and $Z_{gp}(s)$ when SCL = 50%. (b) Measurement results of $Z_{sn}(s)$ and $Z_{gn}(s)$ when SCL = 50%.

As seen in Fig. 16, when SCL = 0, the impedance of VSG and series-compensated network, both are inductive in the low-frequency areas. By adding the proposed active-damping control, the output impedance of VSG is reshaped from the inductance to the resistance–inductance in the low-frequency areas, as shown in Fig. 17. Meanwhile, when SCL = 50%, the impedance of the series-compensated network is capacitive in the low-frequency areas. From Figs. 16 and 17, the experimental results are in good agreement with the decoupling impedance model. Therefore, the decoupling impedance model is accurate enough to analyze the SSR problem.

Fig. 18 shows the experimental results of the series-compensated grid-connected system controlled by VSG under different conditions. As seen in Fig. 18(a), when the SCL is increased from 0 to 25%, the series-compensated grid-connected system controlled by VSG appears SSR and then runs stably. From Fig. 18(b), when the SCL is further increased from 25% to 50%, the grid-connected currents $i_{\mathrm{gabc}}$ exhibit obvious SSR, and the series-compensated grid-connected system controlled by VSG changes from stable to unstable. With the increase of

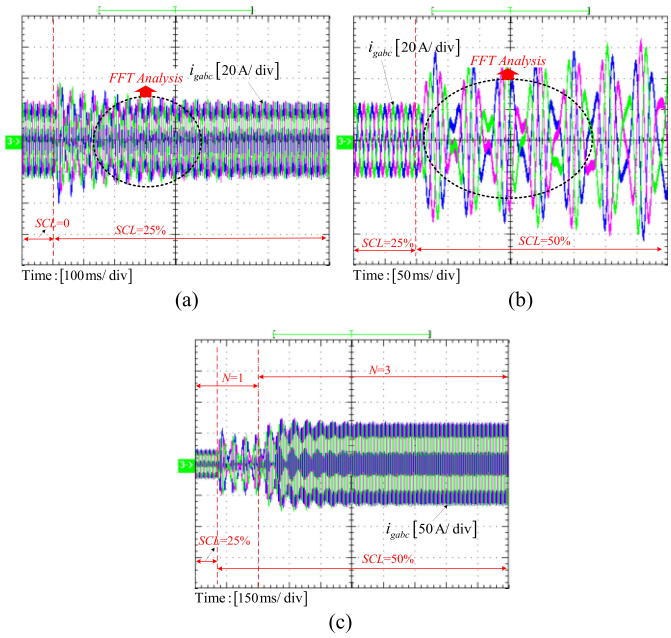


Fig. 18. Experimental results under different conditions. (a) SCL is increased from 0 to 25%. (b) SCL is increased from 25% to 50%. (c) Number $N$ of parallel VSGs is increased from one to three when SCL = 50%.

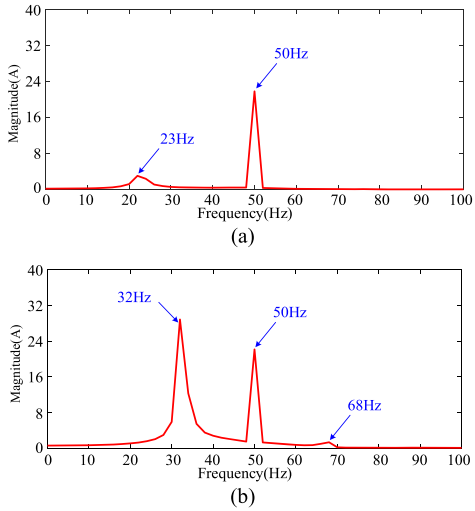


Fig. 19. Spectrum of current in Fig. 18. (a) Current in Fig. 18(a). (b) Current in Fig. 18(b).

SCL, the characteristic capacitance range of the impedance of the series-compensated network becomes bigger, and then it will cause the impedance interaction. As seen in Fig. 18(c), when SCL = 50% and the number $N$ of parallel VSGs is increased from one to three, the SSR can be suppressed and the system can keep stable at last. When the number $N$ of parallel VSGs increases, the parallel impedance of VSGs decreases, the impedance difference of VSGs and series-compensated network becomes bigger, and then it is not easy to cause the impedance interaction and oscillation.

Fig. 19 shows the spectrum of current in Fig. 18. As seen in Fig. 19, when the SCL is increased from 0 to 25%, the

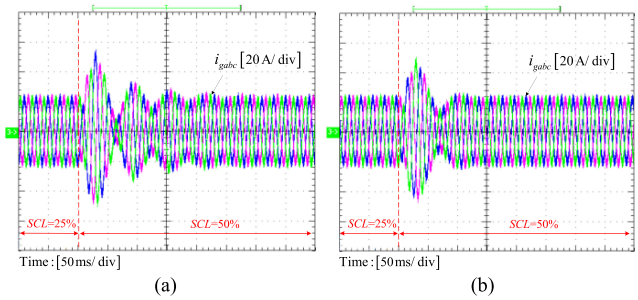


Fig. 20. Experimental waveforms under different values of $R_v$. (a) $R_v = 0.35\ \Omega$. (b) $R_v = 0.7\ \Omega$.

main oscillation frequency is 23 Hz; when the SCL is further increased from 25% to 50%, the main oscillation frequency is 32 Hz. The oscillation frequency becomes higher with the increase of SCL, which is consistent with the theoretical analysis of Fig. 9. From Figs. 18 and 19, with the increase of SCL, the series-compensated grid-connected system controlled by VSG will occur SSR and the induced oscillation frequency becomes higher, which is similar to the SSR characteristics of the series-compensated grid-connected system based on SG [15]. In addition, compared with the SSR of SG under the series-compensated grid-connected situation [16], this SSR does not cause significant supersynchronous oscillation.

Fig. 20 shows the experimental results with the proposed active-damping control. As seen in Fig. 20, the series-compensated grid-connected system controlled by VSG can maintain stable operation when SCL = 50%. In addition, when the value of $R_v$ is bigger, the adjustment time of the system is shorter and the ability to suppress this SSR is stronger. With the increase of $R_v$, the resistance characteristics of VSG becomes stronger in the low-frequency areas, and then the SSR damping ability becomes stronger. As seen in Fig. 20, the proposed active-damping control can effectively suppress the SSR caused by the impedance interaction between the VSG and the series-compensated network. Based on the analysis mentioned above, the experimental results are consistent with the simulation results and the theoretical analysis, which prove the validity of the proposed active-damping control strategy.

In addition, to analyze the influence of the proposed active-damping control on the regular operation of VSG, the contrast experimental results are given in Fig. 21. As seen in Fig. 21(b), when $\xi = 4.8\%$, the dynamic performance of VSG is basically the same with that of Fig. 21(a). In addition, from the point of view of the waves of active power and reactive power, the steady-state performance of VSG is slightly improved. As seen in Fig. 21(c), when $\xi = 30\%$, the dynamic performance of VSG is worse than those of Fig. 21(a) and (b). Moreover, when the active power reference $P_{\text{set}}$ changes, the response of reactive power is bigger than those of Fig. 21(a) and (b). Therefore, the couplings between the active and reactive power controls enhance with the increase of the virtual resistor $R_v$. As seen in Fig. 21, with the increase of the virtual resistor $R_v$, the regulate

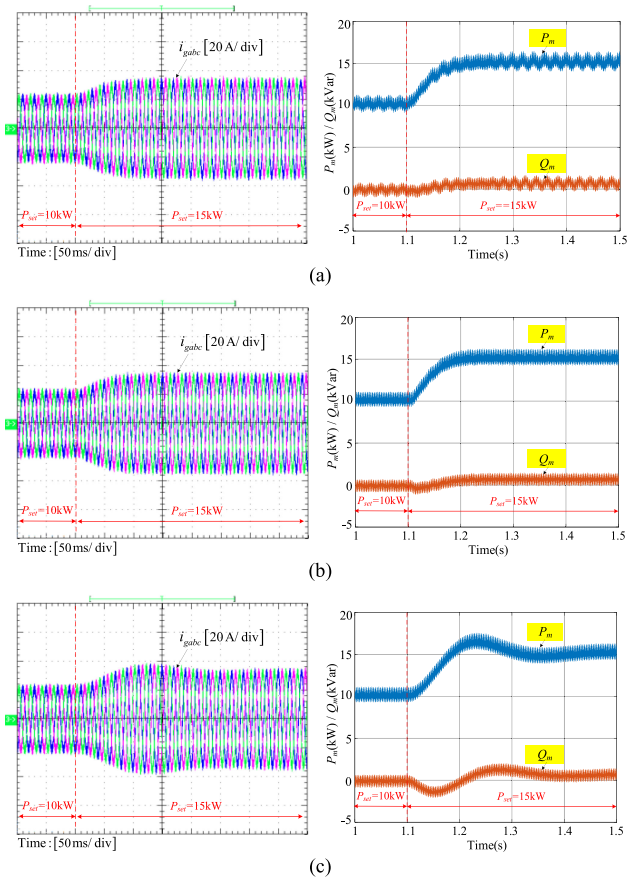


Fig. 21. Performances of VSG under different conditions. (a) Without the proposed active-damping control. (b) With the proposed active-damping control and $\xi = 4.8\%$. (c) With the proposed active-damping control and $\xi = 30\%$.

operation of VSG will be influenced, which is consistent with the analysis in Section III.

## V. Conclusion

This article revealed an SSR phenomenon caused by the impedance interaction between VSG and series-compensated network. Moreover, a modulation signal feedforward active-damping control strategy with time-delay compensation is proposed to suppress this SSR. The conclusions are listed below.

1) The series-compensated grid-connected system controlled by VSG has a similar SSR problem occurred in the traditional series-compensated grid-connected system based on SG. With the increase of SCL, the series-compensated grid-connected system controlled by VSG will appear SSR and the induced oscillation frequency becomes higher, which is similar to the SSR characteristics of the series-compensated grid-connected system based on SG. In addition, compared with the SSR of the series-compensated grid-connected system based on SG, the revealed SSR does not cause significant supersynchronous oscillation. Moreover, with the increase of the parallel VSGs, the stability of the series-compensated grid-connected system controlled by VSG becomes better.

2) The SSR of the series-compensated grid-connected system controlled by VSG can be suppressed by adding a virtual series resistance. In addition, with the increase of the designed virtual series resistance, the damping ability of SSR becomes stronger. Moreover, there is a value range for the virtual series resistance to maintain the regular operation of VSG.
3) Compared with the traditional active-damping control, the proposed modulation signal based active-damping control is independent with the original inverter controller. Therefore, the proposed active-damping control is one universal impedance reshaping control, which can easily be applied to other controllers.

## REFERENCES


[1] T. Bi, J. Li, P. Zhang, E. Mitchell-Colgan, and S. Xiao, "Study on response characteristics of grid-side converter controller of PMSG to sub-synchronous frequency component," *IET Renewable Power Gener.*, vol. 11, no. 7, pp. 966–972, Jun. 2017.

[2] X. Xie, W. Liu, H. Liu, Y. Du, and Y. Li, "A system-wide protection against unstable SSCI in series-compensated wind power systems," *IEEE Trans. Power Del.*, vol. 33, no. 6, pp. 3095–3104, Dec. 2018.

[3] C. Karunanayake, J. Ravishankar, and Z. Y. Dong, "Nonlinear SSR damping controller for DFIG based wind generators interfaced to series compensated transmission systems," *IEEE Trans. Power Syst.*, vol. 35, no. 2, pp. 1156–1165, Mar. 2020.

[4] M. Srinivas, I. Hussain, and B. Singh, "Combined LMS-LMF-based control algorithm of DSTATCOM for power quality enhancement in distribution system," *IEEE Trans. Ind. Electron.*, vol. 63, no. 7, pp. 4160–4168. Jul. 2016.

[5] U. Karaagac, S. O. Faried, J. Mahseredjian, and A.-A. Edris, "Coordinated control of wind energy conversation systems for mitigating subsynchronous interaction in DFIG-based wind farms," *IEEE Trans. Smart Grid.*, vol. 5, no. 5, pp. 2440–2449, Sep. 2014.

[6] Q.-C. Zhong and G. Weiss, "Synchronverters: Inverters that mimic synchronous generators," *IEEE Trans. Ind. Electron.*, vol. 58, no. 4, pp. 1259–1267, Apr. 2011.

[7] H. Wu *et al.*, "Small-signal modeling and parameters design for virtual synchronous generators," *IEEE Trans. Ind. Electron.*, vol. 63, no. 7, pp. 4292–4303, Jul. 2016.

[8] G. Li *et al.*, "Virtual impedance-based virtual synchronous generator control for grid-connected inverter under the weak grid situations," *IET Power Electron.*, vol. 11, no. 13, pp. 2125–2132, Nov. 2018.

[9] Q.-C. Zhong, "Power-electronics-enabled autonomous power systems: Architecture and technical routes," *IEEE Trans. Ind. Electron.*, vol. 64, no. 7, pp. 5907–5918, Jul. 2017.

[10] S. D'Arco and J. A. Suul, "Virtual synchronous machines—Classification of implementations and analysis of equivalence to droop controllers for microgrids," in *Proc. IEEE Grenoble Conf.*, Grenoble, France, Jun. 2013, pp. 1–7.

[11] W. Wu *et al.*, "Sequence impedance modeling and stability comparative analysis of voltage-controlled VSGs and current-controlled VSGs," *IEEE Trans. Ind. Electron.*, vol. 66, no. 8, pp. 6460–6472, Aug. 2019.

[12] M. Amin, Q.-C. Zhong, L. Zhang, Z. Li, and M. Shahidehpour, "Small-signal modeling and analysis of VSM for distributed generation in a weak grid," in *Proc 44th Annu. Conf. IEEE Ind. Electron. Soc.*, Washington, DC, USA, 2018, pp. 1501–1506.

[13] A. Rodríguez-Cabero, J. Roldán-Pérez, and M. Prodanovic, "Virtual impedance design considerations for virtual synchronous machines in weak grids," *IEEE J. Emerg. Sel. Topics Power Electron.*, to be published, doi: 10.1109/JESTPE.2019.2912071.

[14] W. Wu *et al.*, "Sequence-impedance-based stability comparison between VSGs and traditional grid-connected inverters," *IEEE Trans. Power Electron.*, vol. 34, no. 1, pp. 46–52, Jan. 2019.

[15] J. V. Milanovic and A. Adrees, "Identifying generators at risk of SSR in meshed compensated AC/DC power networks," *IEEE Trans. Power Syst*, vol. 28, no. 4, pp. 4438–4447, Nov. 2013.

[16] X. Xie, L. Wang, X. Guo, Q. Jiang, Q. Liu, and Y. Zhao, "Development and field experiments of a generator terminal subsynchronous damper," *IEEE Trans. Power Electron.*, vol. 29, no. 4, pp. 1693–1701, Apr. 2014.

[17] L. Wang, X. Xie, Q. Jiang, H. Liu, Y. Li, and H. Liu, "Investigation of SSR in practical DFIG-based wind farms connected to a series-compensated power system," *IEEE Trans. Power Syst.*, vol. 30, no. 5, pp. 2772–2779, Sep. 2015.

[18] S. Atayde and A. Chandra, "Multiple machine representation of DFIG based grid-connected wind farms for SSR studies," in *Proc. 37th Annu. Conf. IEEE Ind. Electron. Soc.*, 2011, pp. 1468–1473.

[19] R. K. Varma and A. Moharana, "SSR in double-cage induction generator-based wind farm connected to series-compensated transmission line," *IEEE Trans. Power Syst.*, vol. 28, no. 3, pp. 2573–2583, Aug. 2013.

[20] L. Wang, X. Xie, Q. Jiang, H. Liu, Y. Li, and H. K. Liu, "Investigation of SSR in practical DFIG-based wind farms connected to a series compensated power system," *IEEE Trans. Power Syst.*, vol. 30, no. 5, pp. 2772–2779, Sep. 2015.

[21] H. K. Liu, X. Xie, C. Zhang, Y. Li, H. Liu, and Y. Hu, "Quantitative SSR analysis of series-compensated DFIG-based wind farms using aggregated RLC circuit model," *IEEE Trans. Power Syst.*, vol. 32, no. 1, pp. 474–483, Jan. 2017.

[22] L. Fan and Z. Miao, "Nyquist-stability-criterion based SSR explanation for type 3 wind generators," *IEEE Trans. Energy Convers.*, vol. 27, no. 3, pp. 807–809, Sep. 2012.

[23] M. Cespedes and J. Sun, "Impedance modeling and analysis of grid-connected voltage-source converters," *IEEE Trans. Power Electron.*, vol. 29, no. 3, pp. 1254–1261, Mar. 2014.

[24] Y. Xu, H. Nian, T. Wang, L. Chen, and T. Zheng, "Frequency coupling characteristic modeling and stability analysis of doubly fed induction generator," *IEEE Trans. Energy Convers.*, vol. 33, no. 3, pp. 1475–1486, Sep. 2018.

[25] M. K. Bakhshizadeh *et al.*, "Couplings in phase domain impedance modeling of grid-connected converters," *IEEE Trans. Power Electron.*, vol. 31, no. 10, pp. 6792–6796, Oct. 2016.

[26] J. Sun, G. Wang, X. Du, and H. Wang, "A theory for harmonics created by resonance in converter-grid systems," *IEEE Trans. Power Electron.*, vol. 34, no. 4, pp. 3025–3029, Apr. 2019.

[27] G. Li, Y. Chen, A. Luo, and H. Wang, "An enhancing grid stiffness control strategy of STATCOM/BESS for damping sub-synchronous resonance in wind farm connected to weak grid," *IEEE Trans. Ind. Inform.*, to be published, doi: 10.1109/TII.2019.2960863.

[28] K. Sun, W. Yao, J. Fang, X. Ai, J. Wen, and S. Cheng, "Impedance modeling and stability analysis of grid-connected DFIG-based wind farm with a VSC-HVDC," *IEEE J. Emerg. Sel. Topics Power Electron.*, to be published, doi: 10.1109/JESTPE.2019.2901747.

[29] B. Badrzadeh, M. Sahni, Y. Zhou, D. Muthumuni, and A. Gole, "General methodology for analysis of sub-synchronous interaction in wind power plants," *IEEE Trans. Power Syst.*, vol. 28, no. 2, pp. 1858–1869, May 2013.

[30] Y. Zhang, X. Chen, and J. Sun, "Sequence impedance modeling and analysis of MMC in single-star configuration," *IEEE Trans. Power Electron.*, vol. 35, no. 1, pp. 334–346, Jan. 2020.

[31] X. Xie, P. Liu, K. Bai, and Y. Han, "Applying improved blocking filters to the SSR problem of the Tuoketuo power system," *IEEE Trans. Power Syst.*, vol. 28, no. 1, pp. 227–235, Feb. 2013.

[32] M. A. Chowdhury and G. M. Shafiullah, "SSR mitigation of series-compensated DFIG wind farms by a nonlinear damping controller using partial feedback linearization," *IEEE Trans. Power Syst.*, vol. 33, no. 3, pp. 2528–2538, May 2018.

[33] X. Wang, Y. W. Li, F. Blaabjerg, and P. C. Loh, "Virtual-impedance-based control for voltage-source and current-source converters," *IEEE Trans. Power Electron.*, vol. 30, no. 12, pp. 7019–7037, Dec. 2015.

[34] P. Piya and M. Karimi-Ghartemani, "A stability analysis and efficiency improvement of synchronverter," in *Proc. IEEE Appl. Power Electron. Conf. Expo.*, Mar. 2016, pp. 3165–3175.

[35] M. Karimi-Ghartemani, S. A. Khajehoddin, P. Piya, and M. Ebrahimi, "Universal controller for three-phase inverters in a microgrid," *IEEE J. Emerg. Sel. Topics Power Electron.*, vol. 4, no. 4, pp. 1342–1353, Dec. 2016.

[36] J. Roldan-Perez, A. Rodriguez-Cabero, and M. Prodanovic, "Harmonic virtual impedance design for parallel-connected grid-tied synchronverters," *IEEE J. Emerg. Sel. Topics Power Electron.*, vol. 7, no. 1, pp. 493–503, Mar. 2019.

**Gaoxiang Li** was born in Henan, China, in 1990. He received the B.S. degree in electrical engineering and automation from the School of Electrical Engineering and Automation, Henan Polytechnic University, Jiaozuo, China, in 2014, and the M.S. degree in electrical engineering from the College of Information Science and Engineering, Central South University, Changsha, China, in 2017. He is currently working toward the Ph.D. degree in electrical engineering with the College of Electrical and Information Engineering, Hunan University, Changsha, China.

His research interests include power quality control, new energy generation, subsynchronous oscillation suppression.

**Yandong Chen** (Senior Member, IEEE) was born in Hunan, China, in 1979. He received the B.S. and M.S. degrees in instrument science and technology from Hunan University, Changsha, China, in 2003 and 2006, respectively, and the Ph.D. degree in electrical engineering from Hunan University, Changsha, China, in 2014.

He has been a Professor in the College of Electrical and Information Engineering, Hunan University, Changsha, China. His research interests include power electronics for microgrid, distributed generation, power quality, and energy storage.

Dr. Chen was a recipient of the 2014 National Technological Invention Award of China and the 2014 WIPO-SIPO Award for Chinese Outstanding Patented Invention. He is a member of IEEE Power Electronics Society.

**An Luo** (Senior Member, IEEE) was born in Changsha, China, in 1957. He received the B.S. and M.S. degrees in industrial automation from Hunan University, Changsha, China, in 1982 and 1986, respectively, and the Ph.D. degree in fluid power transmission and control from Zhejiang University, Hangzhou, China, in 1993.

From 1996 to 2002, he was a Professor with Central South University, Changsha, China. Since 2003, he has been a Professor with the College of Electrical and Information Engineering, Hunan University, Changsha, China, where he also serves as the Chief of National Electric Power Conversion and Control Engineering Technology Research Center. His research interests mainly include distributed generation, microgrid, and power quality.

Dr. Luo was elected to the Chinese National Academy of Engineering (CNAE) in 2015, the highest honor for scientists and engineers and scientists in China. He was a recipient of the highly prestigious China National Science and Technology Awards in 2006, 2010, and 2014.

**Zhixing He** (Member, IEEE) was born in Hunan, China, in 1989. He received the B.S. degree in information science and engineering from Central South University, Changsha, China, in 2011, and the Ph.D. degree in electrical engineering from Hunan University, Changsha, China, in 2017.

He is currently an Associate Professor of electrical engineering with Hunan University, Changsha. His research interests include power electronics and modular multilevel converters.

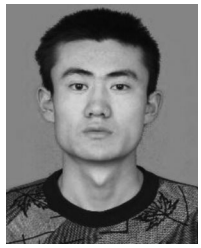

**Haining Wang** was born in Henan, China, in 1992. He received the B.Sc. degree in electrical engineering from Henan Polytechnic University, Jiaozuo, China, in 2015. He is currently working toward the Ph.D. degree in electrical engineering with Hunan University, Changsha, China.

His research interests include power electronics for microgrid, distributed generation, power quality, and energy storage.

**Zhen Zhu** was born in Hunan, China, in 1988. He received the B.S. and M.S. degrees in automation from the College of Geophysics and Information Engineering, China University of Petroleum, Beijing, China, in 2013 and 2017, respectively. He is currently working toward the Ph.D. degree in electrical engineering with the College of Electrical and Information Engineering, Hunan University, Changsha, China, since 2017.

His research interests include hybrid compensation of traction systems and energy management of energy routers.

**Wenhua Wu** (Member, IEEE) was born in Hunan, China, in 1991. He received the B.S. and Ph.D. degrees from the College of Electrical and Information Engineering, Hunan University, Changsha, China, in 2014 and 2019, respectively.

He is currently a Postdoctoral Researcher in electrical engineering with Hunan University, Changsha. His research interests include renewable energy generation systems, microgrids, power quality, and VSC-HVdc systems.

**Leming Zhou** (Member, IEEE) was born in Hunan, China, in 1989. He received the B.S. and Ph.D. degrees in electrical engineering from Hunan University, Changsha, China, in 2011 and 2016, respectively.

He is currently an Associate Professor in electrical engineering with Hunan University, Changsha. His research interests include power electronics, electric power green transformation, distributed generation, and marine special power supply.